Direct observation of chirality-induced spin selectivity in electron donor-acceptor molecules

Direct Observation of Chirality-Induced Spin Selectivity in Electron Donor-Acceptor Molecules

Hannah J. Eckvahl,[1†] Nikolai A. Tcyrulnikov,[1†] Alessandro Chiesa,[2†] Jillian M. Bradley,[1] Ryan M. Young,[1] Stefano Carretta,[2*] Matthew D. Krzyaniak,[1*] and Michael R. Wasielewski[1*]

[1]Department of Chemistry, Center for Molecular Quantum Transduction, and Paula M. Trienens Institute for Sustainability and Energy, Northwestern University, Evanston, IL 60208-3113 USA. [2]Università di Parma, Dipartimento di Scienze Matematiche, Fisiche e Informatiche, Parma, I-43124, Italy.

*Corresponding authors. Email: m-wasielewski@northwestern.edu; mdkrzyaniak@northwestern.edu; stefano.carretta@unipr.it

[†]These authors contributed equally to this work

One-Sentence Summary: The spin dynamics of photogenerated radical pairs are strongly influenced by molecular chirality.

Abstract:
The role of chirality in determining the spin dynamics of photoinduced electron transfer in donor-acceptor molecules remains an open question. Although chirality-induced spin selectivity (CISS) has been demonstrated in molecules bound to substrates, experimental information about whether this process influences spin dynamics in the molecules themselves is lacking. Here we use time-resolved electron paramagnetic resonance spectroscopy to show that CISS strongly influences the spin dynamics of isolated covalent donor-chiral bridge-acceptor (D-Bχ-A) molecules in which selective photoexcitation of D is followed by two rapid, sequential electron transfer events to yield $D^{\bullet+}$-Bχ-$A^{\bullet-}$. Exploiting this phenomenon affords the possibility of using chiral molecular building blocks to control electron spin states in quantum information applications.

Molecules offer a wide variety of quantum properties that could potentially be exploited in qubit architectures for quantum information science (QIS).(*1, 2*) Moreover, molecules afford the ability to tailor these properties as applications dictate, while controlling structure with atomic precision. One such property of growing interest is molecular chirality, which plays an essential role in many chemical reactions and nearly all biological processes. Naaman, Waldeck, and coworkers presented evidence of the relationship between molecular chirality and electron spin (*3, 4*) when they observed that electrons photoemitted from a gold surface coated with a thin film of DNA have a preferred spin state, a phenomenon now known as chirality-induced spin selectivity (CISS).(*5*) Subsequent experiments using molecules bound to metallic, semiconductor, or magnetic substrates have confirmed a connection between electron motion and spin projection along the chiral axis, which is selected to be parallel or antiparallel to the motion, depending on the handedness of the chiral molecule.(*5-9*) The spin selectivity of the effect can be very high, even at room temperature, and its theoretical foundations are still being explored.(*10-17*) However, a key problem hindering a fundamental understanding of CISS is that it is difficult to separate the role of the substrate from that of the chiral molecule.

Hence, it is crucial to investigate how CISS affects electron spin dynamics in molecules undergoing electron transfer that are not bound to substrates. Achieving this understanding would make it possible to design chiral molecular building blocks to manipulate electron spin states, which has potential for QIS applications. In particular, the occurrence of CISS at the molecular level has been proposed as an enabling technology for quantum applications, e.g. solving key issues like single-spin readout and high-temperature spin qubit initialization.(*6*)

Here we show direct evidence of CISS in isolated covalent donor-chiral bridge-acceptor (D-Bχ-A) molecules in which selective photoexcitation of D to its lowest excited singlet state (^{1*}D) is followed by two rapid, sequential electron transfer events: ^{1*}D-Bχ-A → D$^{\bullet+}$-Bχ$^{\bullet-}$-A → D$^{\bullet+}$-Bχ-A$^{\bullet-}$ (Fig. 1A). If formation of D$^{\bullet+}$-Bχ-A$^{\bullet-}$ occurs in ≲1 ns, the resulting entangled electron spin pair is prepared initially in a nearly pure singlet state, ^{1}(D$^{\bullet+}$-Bχ-A$^{\bullet-}$). These states are commonly referred to as spin-correlated radical pairs (SCRPs) and have been studied in systems ranging from photosynthetic proteins(*18-21*) and related model systems(*22-25*) to DNA hairpins.(*26-30*) However, in all these cases, no consideration was given to the possible influence of chirality on the SCRP spin dynamics.

To demonstrate the occurrence of CISS, we have synthesized pairs of covalent D-Bχ-A enantiomers, (*R*)-**1-*h*$_9$** (**-*d*$_9$**) and (*S*)-**1-*h*$_9$** (**-*d*$_9$**), where D is either non-deuterated (**-*h*$_9$**) or fully deuterated (**-*d*$_9$**) *peri*-xanthenoxanthene,(*31*) Bχ is a pair of naphthalene-1,8-dicarboximides that are linked at their 4-positions to form an enantiomeric pair of axially chiral dimers (*R*)-NMI_2 and (*S*)-NMI_2(*32*) and A is naphthalene-1,8:4,5-bis(dicarboximide) (NDI) (see Supplementary Materials, figs. S1-S2). The structures of (*R*)-**1-*h*$_9$** (**-*d*$_9$**) and (*S*)-**1-*h*$_9$** (**-*d*$_9$**) and the corresponding achiral reference molecules **2-*h*$_9$** (**-*d*$_9$**) are shown in Fig. 1B. The enantiomers were separated using HPLC with a chiral stationary phase (fig. S3) and their circular dichroism spectra are given in fig. S4. We have characterized the charge separation and recombination dynamics of these molecules using transient optical absorption (TA) spectroscopy and the CISS effect on their spin dynamics using time-resolved EPR spectroscopy using either continuous (TREPR) or pulsed microwave radiation (pulse-EPR).

We find that CISS yields characteristic features in the TREPR spectra of the photogenerated PXX$^{\bullet+}$- NMI_2-NDI$^{\bullet-}$ SCRP in (*R*)-**1-*h*$_9$** (**-*d*$_9$**) and (*S*)-**1-*h*$_9$** (**-*d*$_9$**), which are absent in achiral **2-*h*$_9$** (**-*d*$_9$**), when the direction of electron transfer is oriented orthogonal to the applied static magnetic

field direction in agreement with simulations. Conversely, the corresponding spectra of PXX$^{\bullet+}$-NMI_2-NDI$^{\bullet-}$ are practically identical when the field is parallel to the electron transfer direction.

Time-resolved EPR Spectroscopy

Samples of (*R*)-**1-*h*$_9$** (**-*d*$_9$**), (*S*)-**1-*h*$_9$** (**-*d*$_9$**), and **2-*h*$_9$** (**-*d*$_9$**) were each prepared in the nematic liquid crystal 4-cyano-4'-(*n*-pentyl)biphenyl (5CB), which was aligned in a magnetic field at 295 K, then rapidly frozen to 85 K, which aligns the long axes of these molecules along the magnetic field. The orientation of the molecules aligned in frozen 5CB can then be rotated relative to the applied magnetic field direction. Since solid 5CB is an optically scattering medium, to assess the photo-driven charge separation dynamics of these molecules at low temperature, we employed both femtosecond and nanosecond transient optical absorption spectroscopy substituting glassy butyronitrile for 5CB at 105 K. Transient absorption spectra and kinetics are given in figs. S5 and S6. The data show that in each case ultrafast two-step charge separation occurs in $\lesssim$ 0.2 ns to give PXX$^{\bullet+}$-NDI$^{\bullet-}$, which recombines to its ground state in τ = 46-66 μs, providing ample time for TREPR measurements. The presence of a ~0.35 T static magnetic field in the TREPR experiments does not affect the ultrafast electron transfer reactions because the Zeeman interaction (~0.3 cm^{-1}) at that field strength is much less than the adiabatic energy gaps (~20-80 cm^{-1}) for these reactions (see table S1 and SM for details).

Pulse-EPR techniques were used to assess the quality of the alignment of (*R*)-**1-*h*$_9$** (**-*d*$_9$**), (*S*)-**1-*h*$_9$** (**-*d*$_9$**), and **2-*h*$_9$** (**-*d*$_9$**) 5CB by measuring the isotropic exchange (J) and dipolar (D) spin-spin interactions for their photogenerated SCRPs, where $D(\theta) = d(1 - 3\cos^2\theta)$ and $d = 52.04\ \mathrm{MHz} \cdot \mathrm{nm}^3/r_{DA}^3$ in the point dipole approximation, which gives detailed distance and orientation information as defined by the Hamiltonian in eq. S3. If photogeneration of the SCRP is followed by a Hahn echo microwave pulse sequence: π/2 pulse - delay τ - π pulse - delay τ - spin echo, and the time delay τ is scanned, coherent oscillations between the eigenstates of the SCRP Hamiltonian $|\Phi_A\rangle$ and $|\Phi_B\rangle$ (see below) that are related to both J and $D(\theta)$ modulate the spin echo amplitude.(*21, 33-37*) When this experiment is performed on spin-coherent SCRPs, the echo appears out-of-phase, *i.e.*, in the detection channel in quadrature to the one in which it is expected, and is therefore termed out-of-phase electron spin echo envelope modulation (OOP-ESEEM).(*21, 33-37*) For large SCRP distances, r_{DA}, J can be neglected and the OOP-ESEEM oscillation frequency is approximately 2d when $\theta = 0°$ and d when $\theta = 90°$. Thus, OOP-ESEEM can be used to measure SCRP distances for a given angle of the dipolar axis relative to the magnetic field.(*28, 36-38*) The dipolar axis in SCRPs connects the centroids of the spin distributions of the two radicals. Figures S7 and S8 show the OOP-ESEEM data for (*R*)-**1-*h*$_9$** (**-*d*$_9$**), (*S*)-**1-*h*$_9$** (**-*d*$_9$**), and **2-*h*$_9$** (**-*d*$_9$**) assuming that their dipolar axes are aligned parallel or perpendicular to the magnetic field. Fitting the OOP-ESEEM data shows that the measured PXX-$h_9$$^{\bullet+}$-NDI$^{\bullet-}$ distances of (*R*)-**1-*h*$_9$**, (*S*)-**1-*h*$_9$**, and **2-*h*$_9$** are 2.48 ± 0.01, 2.48 ± 0.01, and 2.28 ± 0.01 nm, respectively, while the corresponding PXX-$d_9$$^{\bullet+}$-NDI$^{\bullet-}$ distances of (*R*)-**1-*d*$_9$**, (*S*)-**1-*d*$_9$**, and **2-*d*$_9$** are 2.53 ± 0.01, 2.51 ± 0.01, and 2.29 ± 0.02 nm, respectively (table S2). These experimental distances are consistent with the center-to-center distances between PXX and NDI determined from density functional theory calculations on (*R*)-**1-*h*$_9$**, (*S*)-**1-*h*$_9$**, and **2-*h*$_9$**, where r_{DA} = 2.59, 2.60, and 2.40 nm, respectively (fig. S9 and tables S3-S5). The agreement between the experimental and calculated distances shows that the D$^{\bullet+}$-Bχ-A$^{\bullet-}$ SCRPs are well-aligned along the magnetic field direction in frozen 5CB.

The TREPR spectra of aligned (*R*)-**1-*h*$_9$**, (*S*)-**1-*h*$_9$**, and **2-*h*$_9$** were obtained by photoexciting the samples with a 450 nm, 7 ns laser pulse and monitoring the magnetization with continuous microwaves using direct detection (see SM). The spectra obtained 100 ns after the laser pulse (T_{DAF}) are shown in Fig. 2. When the long axes of these molecules are aligned parallel to the

magnetic field direction ($\theta = 0°$), both enantiomers as well as the achiral reference molecule give the same spectra (Figs. 2A and 2C). Rotating the samples so that the long axes of (*R*)-**1-*h*$_9$**, (*S*)-**1-*h*$_9$**, and **2-*h*$_9$** are aligned perpendicular to the magnetic field direction ($\theta = 90°$), results in the appearance of outer wings in the spectra of chiral (*R*)-**1-*h*$_9$** and (*S*)-**1-*h*$_9$** (Fig. 2B). No such enhancement is observed for achiral **2-*h*$_9$**. As explained below, we posit that these new features result from the contribution of CISS to the formation of the SCRPs in (*R*)-**1-*h*$_9$** and (*S*)-**1-*h*$_9$**. Deuteration of PXX$^{\bullet+}$ narrows the overall linewidth of (*R*)-**1-*d*$_9$**, (*S*)-**1-*d*$_9$**, and **2-*d*$_9$**, while retaining the same orientation dependence of the signal (Figs. 2C and 2D).

Effect of CISS on Radical Pair Spin Dynamics

In the molecules described here, the D$^{\bullet+}$-A$^{\bullet-}$ distances are ≳23 Å, so that the spin-spin interactions *J* and *D* are small relative to the ~0.35 T applied magnetic field. Thus, the Zeeman term is by far the leading term in the SCRP spin Hamiltonian (eq. S3), so that the SCRP wavefunctions $|S\rangle = \frac{1}{\sqrt{2}}\,(|\uparrow\downarrow\rangle - |\downarrow\uparrow\rangle)$ and $|T_0\rangle = \frac{1}{\sqrt{2}}\,(|\uparrow\downarrow\rangle + |\downarrow\uparrow\rangle)$, which are magnetic field invariant, remain close in energy, while $|T_{+1}\rangle = |\uparrow\uparrow\rangle$ and $|T_{-1}\rangle = |\downarrow\downarrow\rangle$ are well separated in energy from both $|S\rangle$ and $|T_0\rangle$. In particular, both $|T_{+1}\rangle$ and $|T_{-1}\rangle$ are eigenstates of the spin Hamiltonian, while $|S\rangle$ and $|T_0\rangle$ are not eigenstates because of the different electronic *g*-factors and hyperfine fields of the two spins. Coherent mixing of $|S\rangle$ and $|T_0\rangle$ yields $|\Phi_A\rangle = \cos\phi\,|S\rangle + \sin\phi\,|T_0\rangle$ and $|\Phi_B\rangle = -\sin\phi\,|S\rangle + \cos\phi\,|T_0\rangle$ (Fig. 3A), which are eigenstates of the spin Hamiltonian, where the angle ϕ in the mixing coefficients is derived from the magnetic parameters of the SCRP (see SM).(*39-41*)

In the ultrafast electron transfer regime observed here, the initial spin state for an achiral SCRP is the entangled singlet $|S\rangle$ state yielding populations only on $|\Phi_A\rangle$ and $|\Phi_B\rangle$. Therefore, four allowed transitions occur between them and the initially unpopulated $|T_{+1}\rangle$ and $|T_{-1}\rangle$ states, giving rise to a spin-polarized (out of equilibrium) EPR spectrum. When $\theta = 0°$, this results in a typical (*e*, *a*, *e*, *a*) spin polarization pattern (low to high field, where *a* = enhanced absorption, and *e* = emission) because $D(\theta) < 0$. (*39-41*) Conversely, when $\theta = 90°$, the pattern is reversed (*a*, *e*, *a*, *e*) because $D(\theta) > 0$. Since the *g*-tensors of PXX$^{\bullet+}$ and NDI$^{\bullet-}$ are very similar, i.e. [2.0045, 2.0045, 2.0031](*42*) and [2.0047 2.0047 2.0027],(*43*) respectively, the expected SCRP polarization patterns, (*e*, *a*, *e*, *a*) or (*a, e, a, e*), are reduced to broadened (*e*, *a*) or (*a, e*) patterns, as observed experimentally for the achiral reference molecules **2-*h*$_9$** and **2-*d*$_9$** (Fig. 2, blue traces). Our OOP-ESEEM results show that the dipolar axis of each SCRP is well aligned with the long axis of each molecule so that the dipolar axis and the chirality axis of (*R*)-**1-*h*$_9$** (**-*d*$_9$**) and (*S*)-**1-*h*$_9$** (**-*d*$_9$**) are nearly parallel. The angle θ between this axis and the applied magnetic field (B_0) direction is depicted in Fig. 3B for the parallel and in Fig. 3E for perpendicular orientations. CISS mixes triplet character into the initial singlet SCRP, thus the initial populations of $|\Phi_A\rangle$, $|\Phi_B\rangle$, $|T_{+1}\rangle$ and $|T_{-1}\rangle$ and the corresponding transition intensities are predicted to change as well.(*44-47*) If CISS is the sole contribution to the spin dynamics and $\theta = 0°$ (Fig. 3D), the state following electron transfer would be $|\uparrow\downarrow\rangle$ or $|\downarrow\uparrow\rangle$, depending on the chirality of the enantiomer and whether B_0 is parallel or antiparallel to the electron motion. Given that the typical alignment of linear D-B-A molecules within nematic liquid crystals is not unidirectional, B_0 has equal probability of being parallel or antiparallel to the electron motion and hence, if coherences are lost, the initial state is an equal mixture of $|\uparrow\downarrow\rangle$ and $|\downarrow\uparrow\rangle$, and is thus equivalent to having a pure initial $|S\rangle$ state. This situation is shown schematically in Fig. 3C, where the blue and red traces depict the idealized TREPR spectra expected when CISS contributes 0 and 100%, respectively. Indeed, the observed spectra of both

enantiomers as well as the achiral reference molecule are practically identical for $\theta = 0°$ (Figs. 2A and 2C).

In contrast, when the chirality axis is orthogonal to B_0 (Fig. 3E) the initial state is very different in the presence or absence of CISS. In particular, the CISS contribution initially populates $|T_{+1}\rangle$ and $|T_{-1}\rangle$ (see eq. S12). Therefore, if the SCRP spin state has a 100% CISS contribution, the TREPR spectra have a nearly opposite intensity pattern with respect to the case in which CISS does not contribute. This is illustrated in Fig. 3F where the blue and red lines in the idealized TREPR spectra correspond to the intensity for the pure $|S\rangle$ (I_S) and pure CISS (I_{CISS}) initial conditions, respectively.

Starting from recent theoretical models(*44-47*) describing the influence of CISS on SCRP spin dynamics in cases for which the CISS contribution will not be 100%, the initial state will be a superposition or a mixture of $|S\rangle$ and $|T_0\rangle$ along the chiral axis direction, making the detection of CISS less obvious. In fact, the spectral line intensities in this case are the weighted sum of I_S and I_{CISS}, which occur at the same resonance fields and tend to cancel out (see details in the SM). The key to unraveling CISS and pure singlet contributions to the SCRP spin state in the molecules studied here is the observation of a larger EPR linewidth that occurs when CISS contributes. Indeed, the sum of the two contributions (Fig. 3F, black trace) yields a signal that displays lateral wings of opposite sign and central features that are narrower than those produced in the absence of CISS, exactly as observed experimentally in Figs. 2B and 2D. These features are unambiguous signatures of CISS, because they cannot be produced starting from an initial $|S\rangle$ state, where the polarization pattern is fixed to (a, e) for $\theta = 90°$ by the sign of $D(\theta)$.(*39-41*)

The larger linewidth obtained for the CISS initial state arises from the very different dependence of I_S and I_{CISS} on the degree of coherent mixing in the eigenstates. Indeed, $|I_{CISS}|$ increases with increasing entanglement ($\phi \to 0$) while $|I_S|$ decreases (fig. S10). Exploring the variation of the intensity by varying the composition of the $|\Phi_A\rangle$ and $|\Phi_B\rangle$ eigenstates is made possible by the presence of several nuclear spins and by distributed magnetic parameters, e.g. dipolar couplings, often termed strain. Therefore, moving from the center of each transition, i.e. the center of the distributions of the magnetic parameters and hyperfine fields, to the tail of the lineshape corresponds to changing the composition of the eigenstates, producing different linewidths for different initial states. If entanglement in the eigenstates is larger in the tails of the spectrum, the CISS contributions result in magnetic field dependent broadening, giving rise to lateral contributions to the lineshape of opposite sign with respect to the central features (Fig. 3F, black trace).

To confirm this interpretation, we consider the spectra of partially deuterated (*R*)-**1-*d*$_9$** and (*S*)-**1-*d*$_9$**. By strongly diminishing the hyperfine couplings on one of the two radicals, we change the distribution of the eigenstate composition and probe its effect on the lineshape. The measured spectra for $\theta = 0°$ and $\theta = 90°$ are shown in Figs. 2C and 2D, respectively. While no qualitative effect is visible in the parallel direction as expected, the lateral wings are significantly reduced in the perpendicular orientation. These spectra were simulated using a minimal SCRP model with either one spin-½ nucleus (hydrogen atom) on both $NDI^{\bullet-}$ and PXX^{+} or only on $NDI^{\bullet-}$, the latter of which is the partially deuterated case. For reasonable values of the hyperfine couplings, the simulations shown in Fig. 4 reproduce the experimental behavior.

The intensities of the lateral wings are correctly reproduced by combining I_S and I_{CISS} with weights of 41% and 59%, respectively (Fig. 4). While a 59% CISS contribution is remarkable, it must be stressed that this is a minimal model in which the effect of the nuclei is accounted for only qualitatively and a full spectral simulation with all nuclear spins in the fully protonated molecules is very demanding. However, we have been able to perform the simulation for the deuterated case,

which includes all four ^{1}H and two ^{14}N nuclei coupled to the electron spin in $NDI^{\bullet-}$ and effects of dipolar strain. In this case, the experimental behavior is very well reproduced with a 47% CISS contribution, which is still considerable.

Further evidence for the validity of this interpretation is obtained by investigating the time dependence of the TREPR spectra, which reflect the time evolution of the $D^{\bullet+}$-Bχ-$A^{\bullet-}$ spin states under the combined effect of coherent and incoherent terms as described by the stochastic Liouville equation and the presence of the microwave field (see SM). Indeed, figs. S11 and S12 show that the dependence of the observed intensity of the wings of the spectra are similar to that of the main peaks, in agreement with our numerical simulations.

Interestingly, the CISS contribution to the spin dynamics of (*R*)-**1**-***h*$_9$ (**-*d*$_9$**) and (*S*)-**1**-***h*$_9$ (**-*d*$_9$**) is similar to the ~50% spin polarization recently reported for an axially chiral binaphthalene derivative covalently linked to a gold film deposited on nickel.(*48*) While this single comparison suggests that the observed CISS effect for the binaphthalene attached to the gold surface may be largely due to the chiral molecule, additional comparative work is needed on a variety of systems to warrant such a conclusion.

Conclusions

We have found direct evidence of the CISS effect on the spin dynamics of photogenerated radical ion pairs in molecular electron donor-acceptor molecules. The observation of CISS in these systems affords possibilities both for increasing our understanding of this important phenomenon and for its possible applications. Importantly, these results show that the substrates/electrodes with their possibly large spin-orbit couplings are not needed for CISS to occur and that TREPR spectroscopy can directly access the spin dynamics resulting from CISS. This provides key information to guide theoretical investigations and makes possible many new targeted experimental studies. In addition, observing CISS at the molecular level is the first step required to transform this fundamental phenomenon into an enabling technology for quantum applications.

References and Notes

1. M. Atzori, R. Sessoli, The second quantum revolution: Role and challenges of molecular chemistry. *J. Am. Chem. Soc.* **141**, 11339-11352 (2019).
2. M. R. Wasielewski *et al.*, Exploiting chemistry and molecular systems for quantum information science. *Nat. Rev. Chem.* **4**, 490-504 (2020).
3. K. Ray, S. P. Ananthavel, D. H. Waldeck, R. Naaman, Asymmetric scattering of polarized electrons by organized organic films of chiral molecules. *Science* **283**, 814-816 (1999).
4. R. Naaman, Y. Paltiel, D. H. Waldeck, Chiral molecules and the electron spin. *Nat. Rev. Chem.* **3**, 250-260 (2019).
5. C. D. Aiello *et al.*, A chirality-based quantum leap. *ACS Nano* **16**, 4989-5035 (2022).
6. A. Chiesa *et al.*, Chirality-induced spin selectivity: An enabling technology for quantum applications. *Adv. Mater.* 2300472 (2023).
7. S. H. Yang, R. Naaman, Y. Paltiel, S. S. P. Parkin, Chiral spintronics. *Nat. Rev. Phys.* **3**, 328-343 (2021).
8. R. Naaman, Y. Paltiel, D. H. Waldeck, Chiral induced spin selectivity gives a new twist on spin-control in chemistry. *Acc. Chem. Res.* **53**, 2659-2667 (2020).
9. I. Carmeli, K. S. Kumar, O. Heifler, C. Carmeli, R. Naaman, Spin selectivity in electron transfer in photosystem i. *Angew. Chem., Int. Ed.* **53**, 8953-8958 (2014).

10. J. Fransson, Charge and spin dynamics and enantioselectivity in chiral molecules. *J. Phys. Chem. Lett.* **13**, 808-814 (2022).
11. J. Fransson, Charge redistribution and spin polarization driven by correlation induced electron exchange in chiral molecules. *Nano Lett.* **21**, 3026-3032 (2021).
12. J. Fransson, Vibrational origin of exchange splitting and "chiral-induced spin selectivity". *Phys. Rev. B* **102**, 235416 (2020).
13. J. Fransson, Chirality-induced spin selectivity: The role of electron correlations. *J. Phys. Chem. Lett.* **10**, 7126-7132 (2019).
14. S. Naskar, V. Mujica, C. Herrmann, Chiral-induced spin selectivity and non-equilibrium spin accumulation in molecules and interfaces: A first-principles study. *J. Phys. Chem. Lett.* **14**, 694-701 (2023).
15. A. Dianat *et al.*, Role of exchange interactions in the magnetic response and intermolecular recognition of chiral molecules. *Nano Lett.* **20**, 7077-7086 (2020).
16. C.-Z. Wang, V. Mujica, Y.-C. Lai, Spin Fano resonances in chiral molecules: An alternative mechanism for the ciss effect and experimental implications. *Nano Lett.* **21**, 10423-10430 (2021).
17. M. S. Zoellner, S. Varela, E. Medina, V. Mujica, C. Herrmann, Insight into the origin of chiral-induced spin selectivity from a symmetry analysis of electronic transmission. *J. Chem. Theory Comput.* **16**, 2914-2929 (2020).
18. R. Bittl, G. Kothe, Transient EPR of radical pairs in photosynthetic reaction centers: Prediction of quantum beats. *Chem. Phys. Lett.* **177**, 547-553 (1991).
19. G. Kothe, S. Weber, R. Bittl, E. Ohmes, M. C. Thurnauer, J. R. Norris, Transient EPR of light-induced radical pairs in plant photosystem I: Observation of quantum beats. *Chem. Phys. Lett.* **186**, 474-480 (1991).
20. R. Bittl, A. van der Est, A. Kamlowski, W. Lubitz, D. Stehlik, Time-resolved EPR of the radical pair $P865^{+\cdot}Q_a^{-\cdot}$ in bacterial reaction centers. Observation of transient nutations, quantum beats and envelope modulation effects. *Chem. Phys. Lett.* **226**, 349-358 (1994).
21. S. A. Dzuba, P. Gast, A. J. Hoff, ESEEM study of spin-spin interactions in spin-polarized $P^+Q_a^-$ pairs in the photosynthetic purple bacterium *Rhodobacter sphaeroides* R26. *Chem. Phys. Lett.* **236**, 595-602 (1995).
22. M. R. Wasielewski, G. L. Gaines, III, G. P. Wiederrecht, W. A. Svec, M. P. Niemczyk, Biomimetic modeling of photosynthetic reaction center function: Long-lived, spin-polarized radical ion pair formation in chlorophyll-porphyrin-quinone triads. *J. Am. Chem. Soc.* **115**, 10442-10443 (1993).
23. K. Hasharoni, H. Levanon, S. R. Greenfield, D. J. Gosztola, W. A. Svec, M. R. Wasielewski, Mimicry of the radical pair and triplet states in photosynthetic reaction centers with a synthetic model. *J. Am. Chem. Soc.* **117**, 8055-8056 (1995).
24. D. Carbonera *et al.*, EPR investigation of photoinduced radical pair formation and decay to a triplet state in a carotene−porphyrin−fullerene triad. *J. Am. Chem. Soc.* **120**, 4398-4405 (1998).
25. S. M. Harvey, M. R. Wasielewski, Photogenerated spin-correlated radical pairs: From photosynthetic energy transduction to quantum information science. *J. Am. Chem. Soc.* **143**, 15508-15529 (2021).
26. R. Carmieli, T. A. Zeidan, R. F. Kelley, Q. Mi, F. D. Lewis, M. R. Wasielewski, Excited state, charge transfer, and spin dynamics in DNA hairpin conjugates with perylenediimide hairpin linkers. *J. Phys. Chem. A* **113**, 4691-4700 (2009).

27. R. Carmieli *et al.*, Structure and dynamics of photogenerated triplet radical ion pairs in DNA hairpin conjugates with anthraquinone end caps. *J. Am. Chem. Soc.* **134**, 11251-11260 (2012).
28. J. H. Olshansky, M. D. Krzyaniak, R. M. Young, M. R. Wasielewski, Photogenerated spin-entangled qubit (radical) pairs in DNA hairpins: Observation of spin delocalization and coherence. *J. Am. Chem. Soc.* **141**, 2152-2160 (2019).
29. J. H. Olshansky, J. Zhang, M. D. Krzyaniak, E. R. Lorenzo, M. R. Wasielewski, Selectively addressable photogenerated spin qubit pairs in DNA hairpins. *J. Am. Chem. Soc.* **142**, 3346-3350 (2020).
30. E. R. Lorenzo, J. H. Olshansky, D. S. D. Abia, M. D. Krzyaniak, R. M. Young, M. R. Wasielewski, Interaction of photogenerated spin qubit pairs with a third electron spin in DNA hairpins. *J. Am. Chem. Soc.* **143**, 4625-4632 (2021).
31. J. A. Christensen, J. Zhang, J. Zhou, J. N. Nelson, M. R. Wasielewski, Near-infrared excitation of the *peri*-xanthenoxanthene radical cation drives energy-demanding hole transfer reactions. *J. Phys. Chem. C* **122**, 23364-23370 (2018).
32. M.-T. Chen *et al.*, 1,1'-bi(2-naphthol-4,5-dicarboximide)s: Blue emissive axially chiral scaffolds with aggregation-enhanced emission properties. *Org. Chem. Front.* **6**, 3731-3740 (2019).
33. M. C. Thurnauer, J. R. Norris, An electron spin echo phase shift observed in photosynthetic algae : Possible evidence for dynamic radical pair interactions. *Chem. Phys. Lett.* **76**, 557-561 (1980).
34. K. M. Salikhov, Y. E. Kandrashkin, A. K. Salikhov, Peculiarities of free induction and primary spin echo signals for spin-correlated radical pairs. *Appl. Magn. Res.* **3**, 199-216 (1992).
35. J. Tang, M. C. Thurnauer, J. R. Norris, Electron spin echo envelope modulation due to exchange and dipolar interactions in a spin-correlated radical pair. *Chem. Phys. Lett.* **219**, 283-290 (1994).
36. R. Bittl, S. G. Zech, Pulsed EPR study of spin-coupled radical pairs in photosynthetic reaction centers: Measurement of the distance between $P700^{\cdot+}$ and $A_1^{\cdot-}$ in photosystem I and between $P865^{\cdot+}$ and $Q_a^{\cdot-}$ in bacterial reaction centers. *J. Phys. Chem. B* **101**, 1429-1436 (1997).
37. S. Santabarbara, I. Kuprov, P. J. Hore, A. Casal, P. Heathcote, M. C. W. Evans, Analysis of the spin-polarized electron spin echo of the [$P700^{+}A_1^{-}$] radical pair of photosystem I indicates that both reaction center subunits are competent in electron transfer in cyanobacteria, green algae, and higher plants. *Biochemistry* **45**, 7389-7403 (2006).
38. R. Carmieli, Q. Mi, A. Butler Ricks, E. M. Giacobbe, S. M. Mickley, M. R. Wasielewski, Direct measurement of photoinduced charge separation distances in donor-acceptor systems for artificial photosynthesis using OOP-ESEEM. *J. Am. Chem. Soc.* **131**, 8372-8373 (2009).
39. C. D. Buckley, D. A. Hunter, P. J. Hore, K. A. McLauchlan, Electron spin resonance of spin-correlated radical pairs. *Chem. Phys. Lett.* **135**, 307-312 (1987).
40. G. L. Closs, M. D. E. Forbes, J. R. Norris, Spin-polarized electron-paramagnetic resonance-spectra of radical pairs in micelles - observation of electron spin-spin interactions. *J. Phys. Chem.* **91**, 3592-3599 (1987).
41. A. J. Hoff, P. Gast, S. A. Dzuba, C. R. Timmel, C. E. Fursman, P. J. Hore, The nuts and bolts of distance determination and zero- and double-quantum coherence in photoinduced radical pairs. *Spectrochim. Acta, Part A* **54A**, 2283-2293 (1998).

42. H. Mao, G. J. Pazera, R. M. Young, M. D. Krzyaniak, M. R. Wasielewski, Quantum gate operations on a spectrally addressable photogenerated molecular electron spin-qubit pair. *J. Am. Chem. Soc.* **145**, 6585-6593 (2023).
43. Y. Wu, M. D. Krzyaniak, J. F. Stoddart, M. R. Wasielewski, Spin frustration in the triradical trianion of a naphthalenediimide molecular triangle. *J. Am. Chem. Soc.* **139**, 2948-2951 (2017).
44. T. P. Fay, D. T. Limmer, Origin of chirality induced spin selectivity in photoinduced electron transfer. *Nano Lett.* **21**, 6696-6702 (2021).
45. T. P. Fay, Chirality-induced spin coherence in electron transfer reactions. *J. Phys. Chem. Lett.* **12**, 1407-1412 (2021).
46. J. Luo, P. J. Hore, Chiral-induced spin selectivity in the formation and recombination of radical pairs: Cryptochrome magnetoreception and EPR detection. *New J. Phys.* **23**, 043032 (2021).
47. A. Chiesa *et al.*, Assessing the nature of chiral-induced spin selectivity by magnetic resonance. *J. Phys. Chem. Lett.* **12**, 6341-6347 (2021).
48. D. Amsallem, A. Kumar, R. Naaman, O. Gidron, Spin polarization through axially chiral linkers: Length dependence and correlation with the dissymmetry factor. *Chirality* **35**, 562-568 (2023).
49. H. J. Eckvahl *et al.,* Direct observation of chirality-induced spin selectivity in electron donor-acceptor molecules. Dryad: doi.org/10.5061/dryad.fbg79cp1r (2023).
50. A. Sciutto *et al.*, Customizing photoredox properties of PXX-based dyes through energy level rigid shifts of frontier molecular orbitals. *Chem. - Eur. J.* **24**, 4382-4389 (2018).
51. J. L. Sessler *et al.*, A rigid chlorin−naphthalene diimide conjugate. A possible new noncovalent electron transfer model system. *J. Org. Chem.* **63**, 7370-7374 (1998).
52. R. M. Young *et al.*, Ultrafast conformational dynamics of electron transfer in exbox^{4+}⊂perylene. *J. Phys. Chem. A* **117**, 12438-12448 (2013).
53. D. Gosztola, M. P. Niemczyk, W. Svec, A. S. Lukas, M. R. Wasielewski, Excited doublet states of electrochemically generated aromatic imide and diimide radical anions. *J. Phys. Chem. A* **104**, 6545-6551 (2000).
54. S. Stoll, A. Schweiger, Easyspin, a comprehensive software package for spectral simulation and analysis in EPR. *J. Magn. Reson.* **178**, 42-55 (2006).
55. C. E. Tait, M. D. Krzyaniak, S. Stoll, Computational tools for the simulation and analysis of spin-polarized EPR spectra. *J. Magn. Reson.* **349**, 107410 (2023).
56. Y. Shao *et al.*, Advances in molecular quantum chemistry contained in the Q-Chem 4 program package. *Mol. Phys.* **113**, 184-215 (2015).
57. P. J. Hore, in *Advanced EPR in biology and biochemistry,* A. J. Hoff, Ed. (Elsevier, Amsterdam, 1989), pp. 405-440.
58. A. Weller, Photoinduced electron transfer in solution: Exciplex and radical ion pair formation free enthalpies and their solvent dependence. *Z. Phys. Chem.* **133**, 93-99 (1982).
59. H. Mao, R. M. Young, M. D. Krzyaniak, M. R. Wasielewski, Controlling the dynamics of three electron spin qubits in a donor-acceptor-radical molecule using dielectric environment changes. *J. Phys. Chem. Lett.* **12**, 2213-2218 (2021).
60. G. L. Closs, J. R. Miller, Intramolecular long-distance electron transfer in organic molecules. *Science* **240**, 440-447 (1988).

Acknowledgments:

Funding:
This work was supported by the National Science Foundation under award no. CHE-2154627 (M.R.W., synthesis, transient optical and EPR measurements).
Research supported as part of the Center for Molecular Quantum Transduction, an Energy Frontier Research Center funded by the U.S. Department of Energy (DOE), Office of Science, Basic Energy Sciences (BES), under award DE-SC0021314 (M.D.K., EPR data analysis).
This work was supported by the ERC-Synergy project CASTLE (project no. 101071533) funded by the Horizon Europe Program and the Fondazione Cariparma (S.C., calculations).
^{1}H nuclear magnetic resonance (NMR) spectroscopy, and mass spectrometry are conducted in IMSERC facilities at Northwestern University, which have received support from the Soft and Hybrid Nanotechnology Experimental (SHyNE) Resource (NSF ECCS-2025633), NSF CHE-1048773, Northwestern University, the State of Illinois, and the International Institute for Nanotechnology (IIN).

Author contributions:
Conceptualization: MRW
Methodology: HJE, NAT, JMB, MDK, AC, SC, RMY, MRW
Investigation: HJE, NAT, JMB, MDK, AC, SC, RMY, MRW
Visualization: HJE, NAT, AC, RMY, MRW
Funding acquisition: MRW, SC
Project administration: MRW
Supervision: MRW, MDK, SC
Writing – original draft: MRW, MDK, HJE, NAT, SC, AC
Writing – review & editing: MRW, MDK, HJE, NAT, SC, AC

Competing interests:
Authors declare that they have no competing interests.

Data and materials availability:
All data are available in the main text, the supplementary materials, and in Dryad(*49*).

Supplementary Materials
Materials and Methods
Supplementary Text
Figs. S1 to S12
Tables S1 to S7
References (*50-60*)

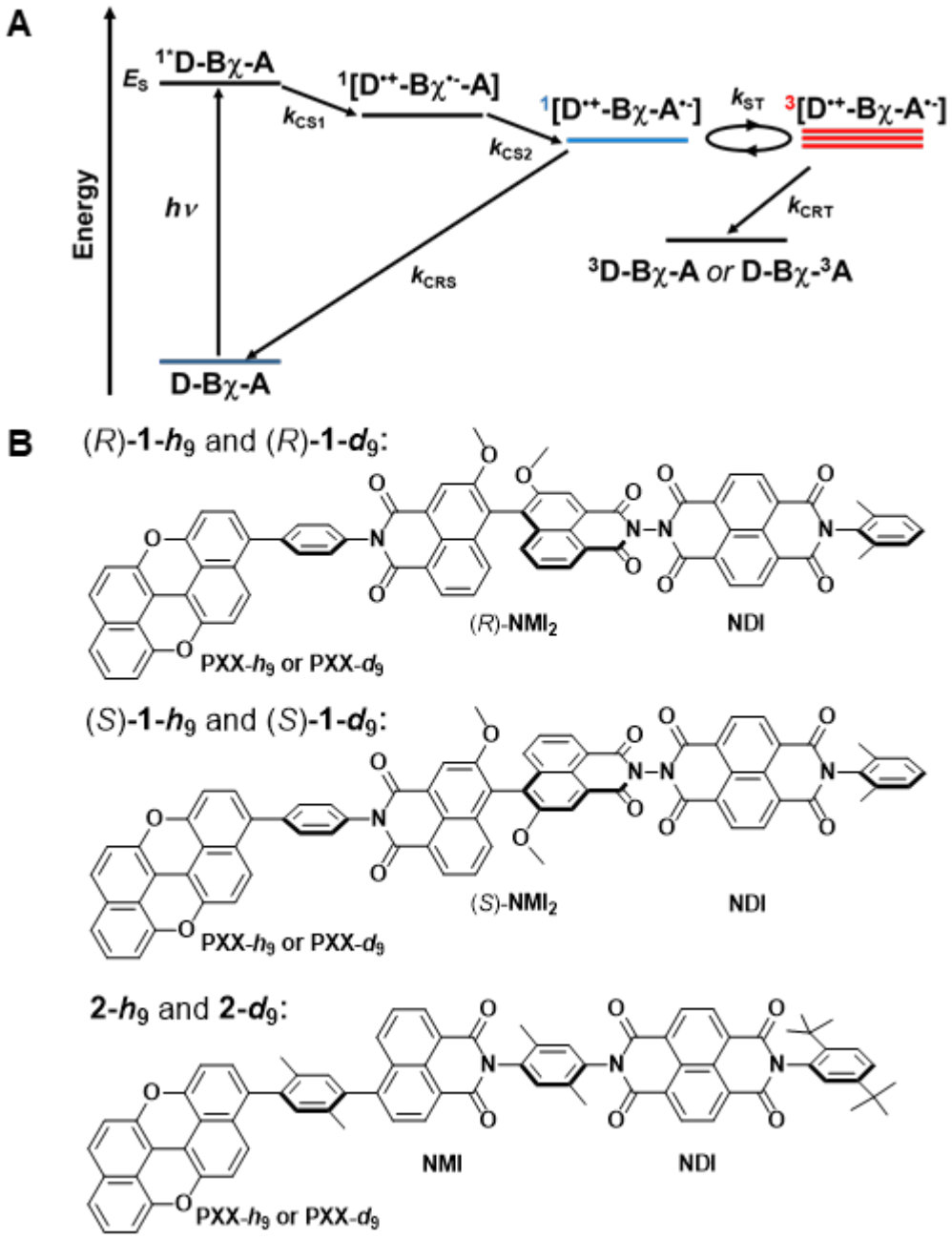

Fig. 1. Electron transfer pathways and molecular structures. (**A**) Electron transfer and intersystem crossing pathways in a D-Bχ-A system with no applied magnetic field, where k_{CS1} and k_{CS2} are the charge separation rate constants, k_{ST} is singlet-triplet mixing rate constant, and k_{CRS} and k_{CRT} are the charge recombination rates via the singlet and triplet channels, respectively. (**B**) Structures of chiral (*R*)-**1** and **(***S*)-**1** and achiral **2**. The steric constraints imposed by linking the two NMI groups in (*R*)-**1** and **(***S*)-**1** result in stable enantiomers having axial chirality.

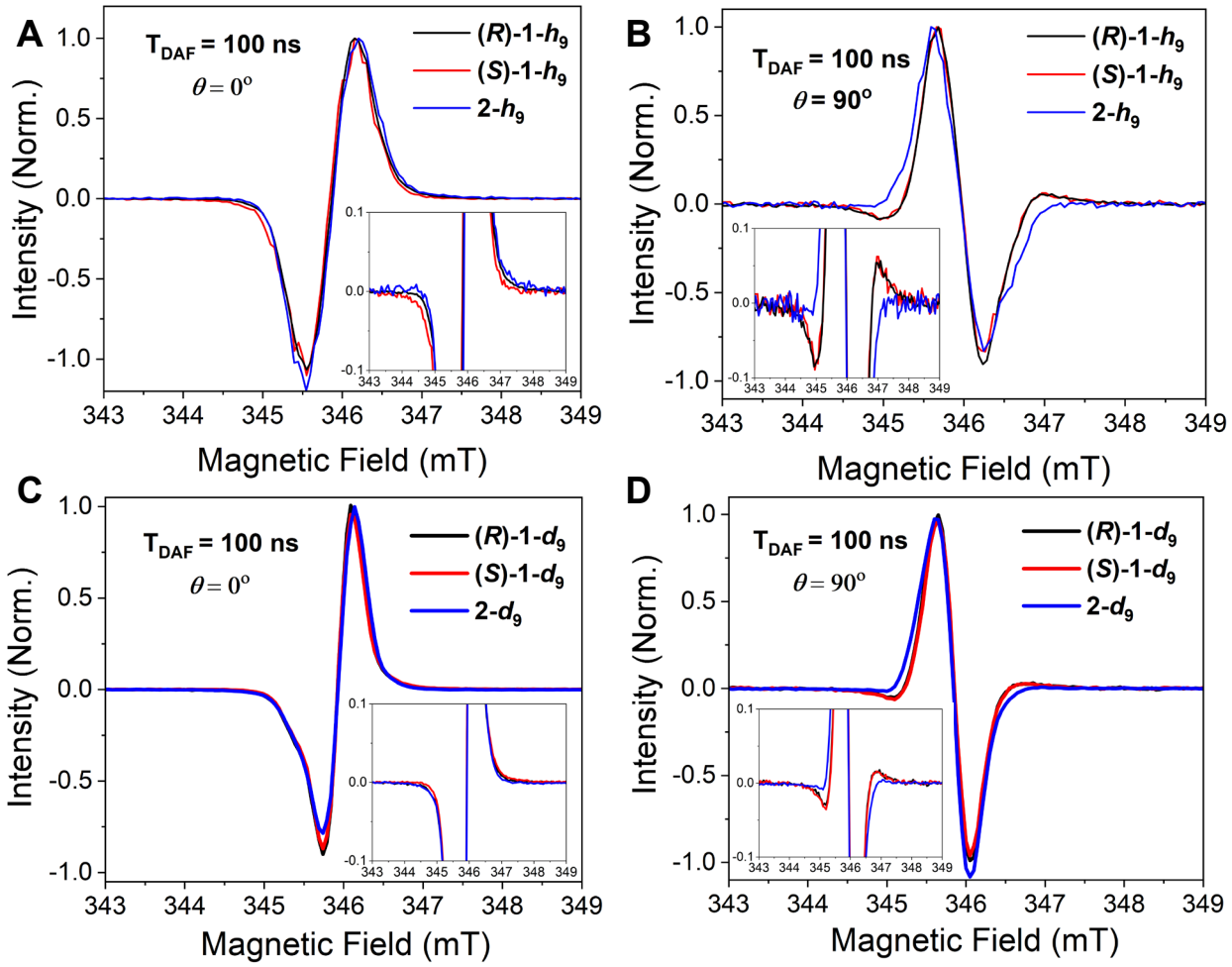

Fig. 2. TREPR spectra. TREPR spectra of (*R*)-**1-*h*$_9$**, (*S*)-**1-*h*$_9$**, and **2-*h*$_9$** (**A**, **B**) and (*R*)-**1-*d*$_9$**, (*S*)-**1-*d*$_9$**, and **2-*d*$_9$** (**C**, **D**) oriented in the nematic liquid crystal 5CB at 85 K and 100 ns after a 450 nm, 7 ns laser pulse with the long axis of each molecule (**A**, **C**) 0° and (**B**, **D**) 90° relative to the applied magnetic field direction. Insets: the spectra are shown with their intensities expanded to highlight features characteristic of CISS.

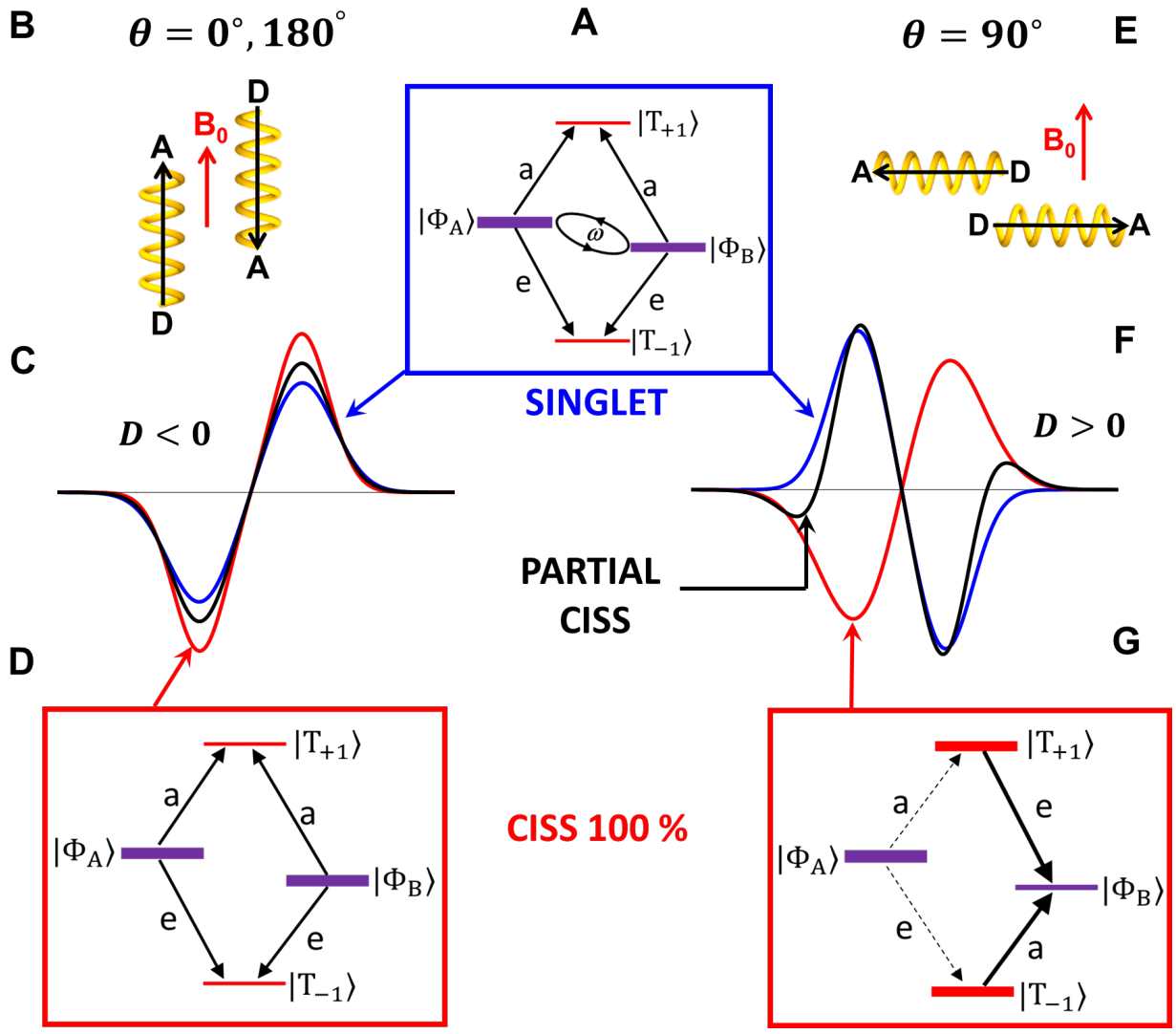

Fig. 3. The CISS effect on the spin states of SCRPs. (**A**) SCRP spin states in the absence of CISS and in the presence of a static magnetic field B_0 that is much greater than J, D, and the hyperfine interactions in both radicals for a singlet precursor. The enhanced absorptive (a) and emissive (e) microwave-induced EPR transitions are indicated. (**B**) Schematic of chiral molecules aligned parallel to B_0. (**C**) TREPR spectra with $\theta = 0°$ expected for an achiral SCRP (blue trace) and for a chiral SCRP with an initial state having 100% CISS contribution (red trace) or a partial CISS contribution (black trace). (**D**) SCRP spin states for $\theta = 0°$ where the initial state has a 100% CISS contribution. (**E**) Schematic of chiral molecules aligned perpendicular to B_0. (**F**) TREPR spectra with $\theta = 90°$ expected for an achiral SCRP (blue trace) and for a chiral SCRP with an initial state having 100% CISS contribution (red trace) or a partial CISS contribution (black trace, rescaled). (**G**) SCRP spin states for $\theta = 90°$ where the initial state has a 100% CISS contribution. The width of the energy levels in (**A**), (**D**), and (**G**) indicates the population of the initial state, while the relative arrow thicknesses in the boxes depict the transition probabilities.

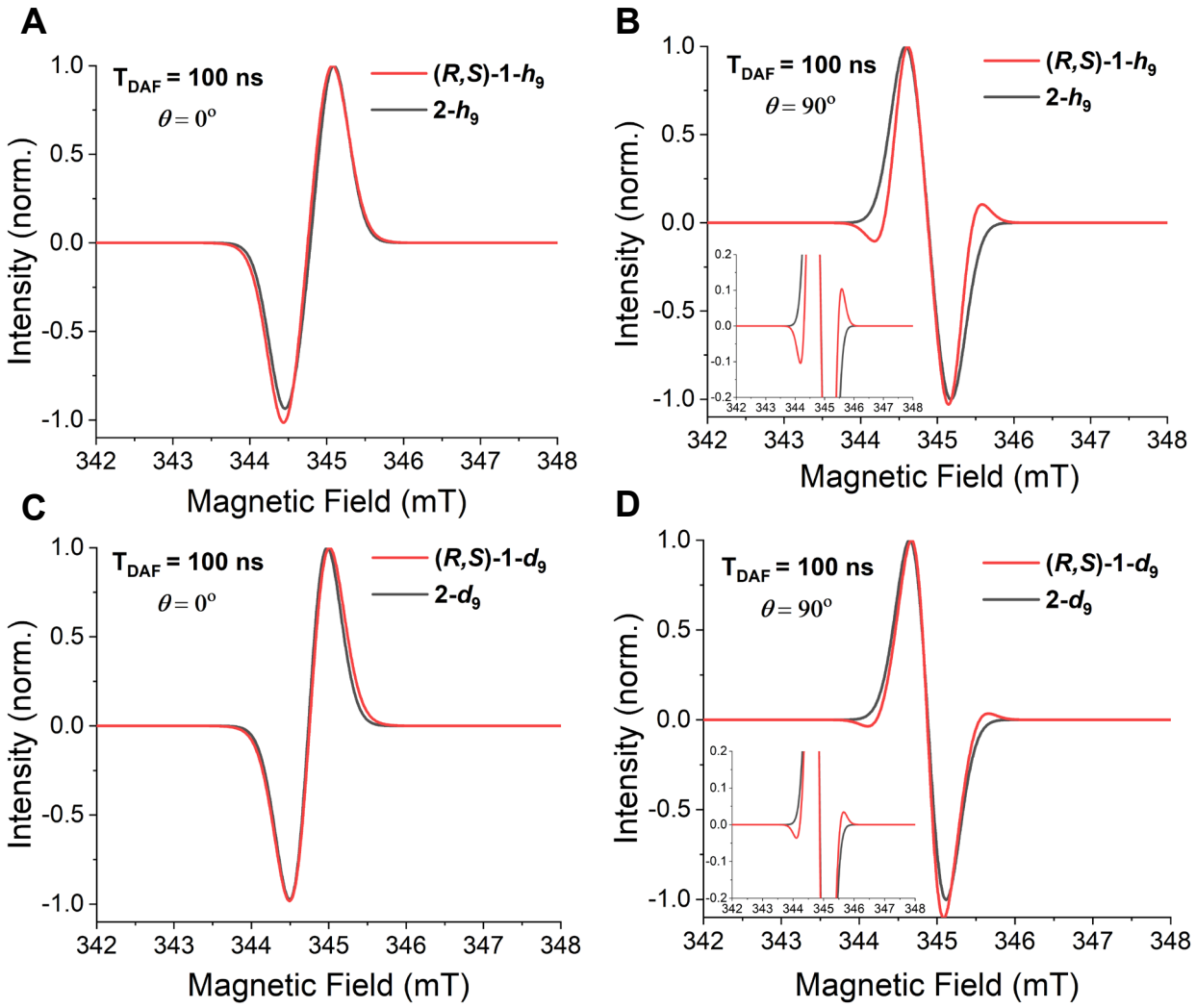

Fig. 4. Simulations of the TREPR spectra with a minimal model of the SCRP. The model places one hydrogen nuclear spin-½ on both $PXX^{\bullet+}$ and $NDI^{\bullet-}$ (**A**, **B**) or only on $NDI^{\bullet-}$ (**C**, **D**). The nuclear spins are coupled to each radical with isotropic hyperfine couplings $a_{\mathrm{NDI}} = 6.3$ MHz and $a_{\mathrm{PXX}} = 10$ MHz. Insets: the simulations are shown with their intensities expanded to highlight features characteristic of CISS. The complete list of simulation parameters is given in table S7.